

Near/Far-Field Channel Estimation For Terahertz Systems With ELAAs: A Block-Sparse-Aware Approach

Hongwei Wang, Jun Fang, Huiping Duan, Hongbin Li, *Fellow, IEEE*

Abstract—Millimeter wave/Terahertz (mmWave/THz) communication with extremely large-scale antenna arrays (ELAAs) offers a promising solution to meet the escalating demand for high data rates in next-generation communications. A large array aperture, along with the ever increasing carrier frequency within the mmWave/THz bands, leads to a large Rayleigh distance. As a result, the traditional plane-wave assumption may not hold valid for mmWave/THz systems featuring ELAAs. In this paper, we consider the problem of hybrid near/far-field channel estimation by taking spherical wave propagation into account. By analyzing the coherence properties of any two near-field steering vectors, we prove that the hybrid near/far-field channel admits a block-sparse representation on a specially designed orthogonal dictionary. Specifically, the percentage of nonzero elements of such a block-sparse representation decreases in the order of $1/\sqrt{N}$, which tends to zero as the number of antennas, N , grows. Such a block-sparse representation allows to convert channel estimation into a block-sparse signal recovery problem. Simulation results are provided to verify our theoretical results and illustrate the performance of the proposed channel estimation approach in comparison with existing state-of-the-art methods.

Index Terms—Hybrid near/far-field, extremely large-scale antenna array, channel estimation.

I. INTRODUCTION

Millimeter wave (mmWave) and extremely large-scale antenna arrays (ELAAs) are two key enabling technologies for the next-generation mobile communications to enhance the system capacity and coverage [1]–[3]. Implementing these physical-layer technologies will lead to a fundamental shift in characteristics of electromagnetic wave propagation, which in turn affects the modeling approach for channels. With the increase of the number of antennas at the base stations (BS) and the decrease of the signal wavelength, the Rayleigh distance of the antenna array, which is considered as a boundary between the radiating near-field region and the far-field region, may extend to several dozen meters. Consequently, the user equipment (UE) may be located in either the near-field or the far-field region. This renders the well-known plane wave assumption, valid only for the far-field region, incompetent for correctly characterizing the hybrid near/far-field channel.

Hongwei Wang, and Jun Fang are with the National Key Laboratory of Wireless Communications, University of Electronic Science and Technology of China, Chengdu 611731, China, Email: JunFang@uestc.edu.cn

Huiping Duan is with the School of Information and Communications Engineering, University of Electronic Science and Technology of China, Chengdu 611731, China, Email: huipingduan@uestc.edu.cn

Hongbin Li is with the Department of Electrical and Computer Engineering, Stevens Institute of Technology, Hoboken, NJ 07030, USA, E-mail: Hongbin.Li@stevens.edu

Channel state information (CSI) acquisition is a prerequisite for optimizing wireless communication systems. Accurate CSI is vital to realize the full potential of ELAAs. The CSI can be obtained via the well-known least squares (LS) method [4]–[6], provided that the length of the pilot sequence is larger than the dimension of the channel (typically equivalent to the number of antennas at the BS). However, in scenarios with ELAAs, the traditional LS based channel estimation method requires a large number of pilot symbols, making it impractical for practical systems.

To alleviate the excessive training overhead issue, the inherent sparse structure of mmWave/THz channels should be exploited. Real-world measurements in dense-urban propagation environments reveal that mmWave/THz channels exhibit a sparse structure in the angular domain. By utilizing this property, the well-known OMP algorithm was employed [7]–[9] to estimate the channel, which is sparsely represented via the standard Fourier transform. In addition, the sparse Bayesian learning [10], [11] as well as the message passing algorithms [12]–[14] were utilized to further improve the channel estimation accuracy. Furthermore, to mitigate the performance degradation caused by grid mismatch, the atomic norm minimization based gridless compressive sensing algorithm [15] and an iterative reweighted “super-resolution” compressive sensing approach [16] were developed. In addition, the low-rank property of the channel has been considered as another important structure for reducing the training overhead. In [17], the channel was represented by a tensor and then estimated via a CP-decomposition-based method. The low-rank and the sparsity were simultaneously leveraged to devise the channel estimation method [18].

The aforementioned channel estimation methods, however, cannot be directly applied to hybrid near/far-field channels. This is because, unlike the far-field channel model, the hybrid near/far-field channel is characterized by two parameters, namely, the spatial angle and the distance. The near-field channel estimation was studied in [19], where a sparse representation of the near-field channel was investigated in the two-dimensional angular-range domain, also referred to as the polar domain. This sparsity in the polar domain allows to convert near-field channel estimation into a compressed sensing problem. However, joint sampling over this two-dimensional domain results in a sparsifying dictionary with a large number of atoms, leading to an increased computational complexity. Also, due to the correlation among near-field steering vectors, the dictionary exhibits an unsatisfactory restricted isometry

property (RIP) that has a detrimental effect on the channel estimation performance. An extension of the research [19] was presented in [20], which explored the co-existence of near-field and far-field channels. The far-field components and the near-field components were estimated separately, leveraging prior information on the number of paths for each channel type. Nevertheless, such prior knowledge is typically unavailable in real-world scenarios. Moreover, based on the polar-domain channel modeling approach, deep learning techniques were developed for near-field channel estimation [21]–[23].

In addition to the polar-domain channel model, a hybrid spherical- and planar-wave channel model (HSPM) was proposed in [24]–[26] via a sub-array partitioning scheme. Specifically, the ELAA is divided into several virtual sub-arrays, and the number of antenna of each sub-array is small enough such that the well-known planar-wave assumption is valid. In the HSPM framework, the channel estimation generally involves two steps [26]. In the first step, the channel of a reference sub-array is estimated based on the far-field channel model. Leveraging the channel parameters obtained in the first step, the hybrid near/far channel can then be more efficiently estimated in the second phase. In addition, another work [24] developed a deep convolutional-neural-network to estimate the channel parameters associated with the reference sub-array, including the channel gain, the spatial angle as well as the distance parameter of each path. Subsequently, utilizing geometric relationships, the entire channel vector can be estimated. Although the HSPM takes both the spherical wave and planar wave into consideration, there is still a lack of sufficient investigation to exploit the inherent channel sparsity of the hybrid near/far-field channel.

In this paper, we provide an in-depth study of the coherence between any two near-field steering vectors. Based on the derived results, we show that as the number of antennas N increases, near-field channels exhibit a block-sparse representation on a specially designed unitary matrix that is a product of a diagonal matrix and the Discrete Fourier Transform (DFT) matrix. Specifically, our analysis indicates that the percentage of nonzero entries in the beam-space channel vector is at the order of $1/\sqrt{N}$, which tends to zero as N grows. This property allows to exploit the block-sparse structure inherent in near-field channels. Consequently, hybrid near/far-field channel estimation is converted into a block-sparse signal recovery problem that can be efficiently solved by many existing compressed sensing methods. Compared with the polar-domain representation, our new representation usually leads to a well-conditioned measurement matrix more amiable for compressive sensing, which helps achieve a performance improvement as well as an improved computational efficiency.

The current work is an extension of our prior conference paper [27]. In the current work, we provide a more comprehensive analysis of the coherence of near-field steering vectors, some of which were not considered/included in our prior work. In addition, we provide a theoretical analysis of the block-RIP condition of the constructed measurement matrix, which serves as a basis for analyzing the sample complexity of the compressed sensing methods. This part is also missing in our previous work.

The rest of the paper is organized as follows. Section II presents the system model and the hybrid near/far-field channel model. In Section III, we introduce a new unitary matrix for hybrid near/far-field channel representation. In Section IV and Section V, we conduct theoretical analyses and show that the near/far channel admits a block-sparse representation on the specially constructed unitary matrix. Section VI develops a channel estimation approach based on the previous results and analyzes the block-RIP condition for the compressed sensing problem. Simulation results are provided in Section VII, followed by concluding remarks in Section VIII.

II. SYSTEM MODEL AND PROBLEM FORMULATION

A. System Model

We consider a downlink communication scenario, where a BS equipped with an extremely large-scale uniform linear array (ULA) serves multiple single-antenna users. Note that for the downlink channel estimation problem, each user estimates its own channel based on its received signal. Therefore, in the following, we only focus on the channel estimation of a single user. The received signal at the t th time instant for a specific user can be expressed as

$$y_t = \mathbf{h}^H \mathbf{f}_t + n_t \quad (1)$$

where $\mathbf{h} \in \mathcal{C}^{N \times 1}$ denotes the channel from the BS to the user, $\mathbf{f}_t \in \mathcal{C}^{N \times 1}$ is the transmitted signal, and $n_t \sim \mathcal{CN}(0, \sigma^2)$ is the additive complex Gaussian noise. Define $\mathbf{y} \triangleq [y_1 \cdots y_T]^H$, $\mathbf{F} \triangleq [\mathbf{f}_1 \cdots \mathbf{f}_T]^H$, and $\mathbf{n} \triangleq [n_1 \cdots n_T]^H$. We can express the received signal as

$$\mathbf{y} = \mathbf{F}\mathbf{h} + \mathbf{n} \quad (2)$$

The objective of this work is to estimate \mathbf{h} by leveraging the received noisy observations \mathbf{y} .

B. Channel Model

Theoretically, \mathbf{h} can be estimated via a least squares (LS) method provided that the number of observations T is no less than N . Nevertheless, N is in general a large number for extremely large-scale antennas. Hence the LS-based channel estimation method may incur a prohibitively high training overhead. Therefore, the inherent structure of \mathbf{h} should be exploited to reduce the training overhead.

According to the electromagnetic theory, the electromagnetic field can be divided into three regions, i.e., the reactive near-field region, the radiating near-field region, and the far-field region. The Fresnel distance, denoted by Z_1 , is used to characterize the boundary between the reactive near-field and the radiating near-field, while the Rayleigh distance, denoted by Z_2 , is used to characterize the boundary between the near field and far field:

$$Z_1 \triangleq 0.62\sqrt{\frac{D^3}{\lambda}}, \quad Z_2 \triangleq \frac{2D^2}{\lambda} \quad (3)$$

where D is the array aperture and λ is the wavelength.

For conventional massive MIMO systems with a moderate number of antennas, the Rayleigh distance is usually small such that users are always located in the far-field region

of the BS. For example, for a system with 8 antennas and operating at 3.5GHz, the corresponding Rayleigh distance is about 2.1m. Under such a circumstance, the planar wave assumption usually holds valid, which leads to the classical far-filed channel model

$$\mathbf{h} = \sum_{l=1}^L \tilde{g}_l e^{-j\frac{2\pi}{\lambda} r_l} \mathbf{a}(\theta_l) \triangleq \sum_{l=1}^L g_l \mathbf{a}(\theta_l) \quad (4)$$

where L is the number of signal paths, $g_l \triangleq \tilde{g}_l e^{-j\frac{2\pi}{\lambda} r_l}$ with \tilde{g}_l and r_l denoting the channel gain and the distance between the BS and the scatterer/user respectively, θ_l is the angle-of-departure (AoD) of the l th path, and $\mathbf{a}(\theta_l)$ denotes a far-field steering vector given as

$$\mathbf{a}(\theta) \triangleq \frac{1}{\sqrt{N}} \left[1 \quad \dots \quad e^{j\frac{2\pi}{\lambda} (n-1)d \sin(\theta)} \quad \dots \quad e^{j\frac{2\pi}{\lambda} (N-1)d \sin(\theta)} \right]^T$$

where d denotes the distance between neighboring antennas.

For extremely large-scale massive MIMO systems, hundreds or even thousands of antennas may be deployed at the BS. Consider a mmWave system operating at 100GHz and equipped with 256 antennas. It can be calculated that the Fresnel distance is around 2.7m, and the Rayleigh distance is approximately 97.5m. From this example, it is safely to assume that the user/scatterer is usually located beyond the Fresnel distance, i.e. $r_l \geq Z_1$. On the other hand, the user could be very likely located within the Rayleigh distance, i.e. $r_l < Z_2$. Therefore, the spherical wave assumption should be adopted to characterize the channel. Here we adopt a geometric channel model to characterize the hybrid near/far-field channel

$$\mathbf{h} = \sum_{l=0}^{L-1} \tilde{g}_l e^{-j\frac{2\pi}{\lambda} r_l} \mathbf{a}(\theta_l, r_l) \triangleq \sum_{l=0}^{L-1} g_l \mathbf{a}(\theta_l, r_l) \quad (5)$$

where $l = 0$ denotes the line-of-sight (LOS) path; $l = 1, \dots, L-1$ represents the NLOS paths; r_l denotes the distance between the first antenna at the BS (which is considered as the reference antenna) and the user/scatterer associated with the l th path; and $\mathbf{a}(\theta, r)$ denotes a near-field steering vector which depends not only on the angle but also on the distance. Specifically, $\mathbf{a}(\theta, r)$ has the following expression:

$$\mathbf{a}(\theta, r) \triangleq \frac{1}{\sqrt{N}} \left[e^{-j\frac{2\pi}{\lambda} (r^{(1)}-r)} \quad \dots \quad e^{-j\frac{2\pi}{\lambda} (r^{(N)}-r)} \right]^T \quad (6)$$

where λ is the wavelength of the carrier signal, and $r^{(n)}$ denotes the distance between the n th antenna and the scatterer/user. The schematic diagram of $r^{(n)}$ and r is plotted in Fig. 1, from which we can obtain the relationship between $r^{(n)}$ and r as

$$\begin{aligned} r^{(n)} &= \sqrt{r^2 + (n-1)^2 d^2 - 2r(n-1)d \sin(\theta)} \\ &= r\sqrt{1 + \Delta} \end{aligned} \quad (7)$$

where Δ is given by

$$\begin{aligned} \Delta &\triangleq \frac{(n-1)^2 d^2}{r^2} - \frac{2(n-1)d \sin(\theta)}{r} \\ &< \left(\frac{(N-1)d}{r} + 1 \right)^2 - 1 \end{aligned} \quad (8)$$

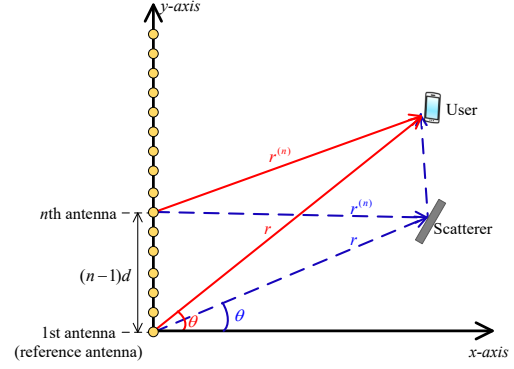


Fig. 1: Schematic diagram of $r^{(n)}$

It should be noticed that $D = (N-1)d$ is the length of the array, which is far smaller than r in general. To justify this, note that we generally assume $r \geq Z_1 = 0.62D\sqrt{D/\lambda} = 0.62\sqrt{(N-1)/2}D$ to ensure that the distance r goes beyond the reactive (inductive) near-field. When $N \geq 256$, we have $r \geq 7D$, in which case the array aperture is relatively small compared with r . Therefore, Δ is usually a small value. Applying the approximation $\sqrt{1+x} \approx 1 + 0.5x$ in (7), which holds for x with small values, results in the following expression for $r^{(n)}$:

$$r^{(n)} \approx - (n-1)d \sin(\theta) + r + \frac{(n-1)^2 d^2}{2r} \quad (9)$$

It should be noted that $r^{(1)} \equiv r$ since the first antenna is treated as a reference antenna.

From (9) we can see that $r^{(n)}$ contains two parts, i.e., an angle-dependent part and a distance-dependent part. Therefore, we can approximate $\mathbf{a}(\theta, r)$ as

$$\mathbf{a}(\theta, r) = \mathbf{a}(r) \circ \mathbf{a}(\theta) \quad (10)$$

where \circ represents the Hadamard product, $\mathbf{a}(\theta)$ is the far-field steering vector, and $\mathbf{a}(r)$ is the distance-dependent term given by

$$\mathbf{a}(r) \triangleq \left[1 \quad \dots \quad e^{-j\frac{2\pi}{\lambda} \left(\frac{(n-1)^2 d^2}{2r} \right)}, \quad \dots \quad e^{-j\frac{2\pi}{\lambda} \left(\frac{(N-1)^2 d^2}{2r} \right)} \right]^T$$

III. SPARSE REPRESENTATION OF HYBRID NEAR/FAR-FIELD CHANNELS

Owing to the sparsity in the angular domain, the far-field channel can be sparsely represented by the spatial Fourier transform matrix [28]. For near-field channels, since it is dependent not only on the angle but also on the distance, a polar-domain sparse representation was introduced in [19], in which a polar-domain transform matrix is constructed by simultaneously sampling different angles and distances. Such a polar-domain channel representation, however, contains a significant number of atoms. In addition, these atoms are not orthogonal to each other, which leads to an ill-conditioned sensing matrix with a relatively large mutual coherence.

To address this issue, in this paper, we attempt to find a new sparse representation for hybrid near/far-field channels that facilitates channel estimation for extremely large-scale massive MIMO systems. Inspired by (10), we define a new unitary matrix

$$\mathbf{D}_{r_p} = \text{diag}(\mathbf{a}(r_p))\mathbf{D} \quad (11)$$

where r_p is a specific distance and $\mathbf{D} \in \mathbb{C}^{N \times N}$ is a discrete Fourier transform (DFT) matrix with its n th column given by $\mathbf{a}(\theta_n)$ with $\sin(\theta_n) = (2n - N - 1)/N$ ($n = 1, \dots, N$). Note that the n th column of \mathbf{D}_{r_p} is equal to $\mathbf{a}(r_p) \circ \mathbf{a}(\theta_n)$, which is an approximation of a near-field steering vector with distance r_p and angle θ_n .

Since $\mathbf{a}(r_p)$ is a constant modulus vector, it can be easily verified that \mathbf{D}_{r_p} is a unitary matrix

$$\mathbf{D}_{r_p}^H \mathbf{D}_{r_p} = \mathbf{D}_{r_p} \mathbf{D}_{r_p}^H = \mathbf{I} \quad (12)$$

Therefore, \mathbf{h} can be uniquely represented by

$$\mathbf{h} = \mathbf{D}_{r_p} \boldsymbol{\alpha}_{r_p} \quad (13)$$

where $\boldsymbol{\alpha}_{r_p}$, the representation of the channel vector on the dictionary \mathbf{D}_{r_p} , is given by

$$\boldsymbol{\alpha}_{r_p} = \sum_{l=0}^{L-1} g_l \mathbf{D}_{r_p}^H \mathbf{a}(\theta_l, r_l) \triangleq \sum_{l=0}^{L-1} g_l \boldsymbol{\alpha}_l \quad (14)$$

with $\boldsymbol{\alpha}_l$ being defined as $\boldsymbol{\alpha}_l \triangleq \mathbf{D}_{r_p}^H \mathbf{a}(\theta_l, r_l)$.

We, in the following, will analyze the inherent structure of $\boldsymbol{\alpha}_{r_p}$. Specifically, we will show that, when N is sufficiently large, $\boldsymbol{\alpha}_{r_p}$ exhibits a block-sparse structure that can be utilized for channel estimation. Due to sparse scattering characteristics, the number of mmWave/THz propagation paths is usually small. To facilitate our analysis, we first consider a simple scenario where there is only an LOS path between the BS and the user. Based on the analysis of this simple case, the extension of our result to the general scenario with multiple paths will be straightforward. In the presence of a single LOS path, $\boldsymbol{\alpha}_{r_p}$ can be simplified as:

$$\boldsymbol{\alpha}_{r_p} = g_0 \boldsymbol{\alpha}_0 \quad (15)$$

where $\boldsymbol{\alpha}_0 = \mathbf{D}_{r_p}^H \mathbf{a}(\theta_0, r_0)$. The structure of $\boldsymbol{\alpha}_{r_p}$ can now be reduced from the structure of $\boldsymbol{\alpha}_0$. Note that each entry of $\boldsymbol{\alpha}_0$ is an inner product of two near-field steering vectors. Therefore to check whether $\boldsymbol{\alpha}_0$ exhibits a certain sparsity structure, we need to study the coherence of two near-field steering vectors.

IV. COHERENCE OF NEAR-FIELD STEERING VECTORS

From $\boldsymbol{\alpha}_0 = \mathbf{D}_{r_p}^H \mathbf{a}(\theta_0, r_0)$, we know that the m th element of $\boldsymbol{\alpha}_0$ is given by

$$\boldsymbol{\alpha}_0(m) = \mathbf{a}^H(\theta_m, r_p) \mathbf{a}(\theta_0, r_0) \quad (16)$$

which indicates that each element in $\boldsymbol{\alpha}_0$ is determined by the coherence of two near-field steering vectors. Define

$$a \triangleq \frac{2\pi d}{\lambda} (\sin(\theta_m) - \sin(\theta_0)) \quad (17)$$

$$b \triangleq \frac{\pi d^2}{\lambda} \left(\frac{1}{r_0} - \frac{1}{r_p} \right) \quad (18)$$

$$\Lambda_n \triangleq (n-1)a + (n-1)^2 b \quad (19)$$

Invoking (10), we have

$$\begin{aligned} f(a, b) &\triangleq \mathbf{a}^H(\theta_m, r_p) \mathbf{a}(\theta_0, r_0) \\ &= \frac{1}{N} e^{-j \frac{2\pi}{\lambda} (r_0 - r_p)} \sum_{n=1}^N e^{-j \Lambda_n} \end{aligned} \quad (20)$$

Therefore, the magnitude of $f(a, b)$ is given by

$$|f(a, b)| = \left| \frac{1}{N} \sum_{n=1}^N e^{-j \Lambda_n} \right| \quad (21)$$

Concerning the value of $|f(a, b)|$, we have the following results when $b = 0$ and when $b \neq 0$.

Proposition 1: When $b = 0$, i.e., $r_0 = r_p$, $|f(a, b)|$ is given by

$$|f(a, b)| = \frac{1}{N} \left| \frac{1 - e^{-jNa}}{1 - e^{-ja}} \right| \quad (22)$$

Proof: When $b = 0$ (i.e., $r_p = r_0$), $f(a, b)$ degenerates into the coherence of two far-field steering vectors, and $|f(a, b)|$ can be obtained as

$$\begin{aligned} |f(a, b)| &= \frac{1}{N} \left| \sum_{n=1}^N e^{-j(n-1)a} \right| \\ &= \frac{1}{N} \left| \frac{1 - e^{-jNa}}{1 - e^{-ja}} \right| \end{aligned} \quad (23)$$

This completes the proof. \blacksquare

Proposition 2: When $b \neq 0$, we have

$$|f(a, b)| \approx \frac{1}{N \sqrt{|b|}} \sqrt{f_1^2(a, b) + f_2^2(a, b)} \quad (24)$$

where $f_1(a, b)$ and $f_2(a, b)$ are, respectively, given as

$$f_1(a, b) \triangleq C \left((N-1)\sqrt{b} + \frac{\tilde{a}}{2\sqrt{b}} \right) - C \left(\frac{\tilde{a}}{2\sqrt{b}} \right) \quad (25)$$

$$f_2(a, b) \triangleq S \left((N-1)\sqrt{b} + \frac{\tilde{a}}{2\sqrt{b}} \right) - S \left(\frac{\tilde{a}}{2\sqrt{b}} \right) \quad (26)$$

$$\tilde{a} \triangleq \text{mod}(a + \pi, 2\pi) - \pi \quad (27)$$

with $C(\zeta) \triangleq \int_0^\zeta \cos(t^2) dt$ and $S(\zeta) \triangleq \int_0^\zeta \sin(t^2) dt$ being, respectively, the Fresnel integrals.

Proof: When $b \neq 0$ (i.e., $r_p \neq r_0$), calculating $|f(a, b)|$ is more complicated. For convenience, we first consider the case where $b > 0$. Define

$$S(a, b) \triangleq \frac{1}{N} \sum_{n=1}^N e^{-j \Lambda_n} \quad (28)$$

Recalling (19), we have

$$S(a, b) = \frac{1}{N} \sum_{n=0}^{N-1} e^{-jan} e^{-jbn^2} \quad (29)$$

$S(a, b)$ is also known as the *generalized quadratic Gauss sums* [29]. To analyze $S(a, b)$, we first consider the two variables a and b . Let $d = \lambda/2$, we have

$$a = \pi(\sin(\theta_m) - \sin(\theta_0)) \quad (30)$$

Clearly, we have $a \in [-2\pi, 2\pi]$. The value of b can be written as

$$b = \frac{\pi\lambda}{4} \left(\frac{1}{r_0} - \frac{1}{r_p} \right) \quad (31)$$

Note that both r_0 and r_p should satisfy

$$r_0, r_p \geq Z_1 \triangleq 0.62\sqrt{\frac{D^3}{\lambda}} \quad (32)$$

since what is of interest is the channel outside the inductive near field region. Therefore, we have

$$\left| \frac{1}{r_0} - \frac{1}{r_p} \right| \leq \frac{1}{0.62} \sqrt{\frac{\lambda}{D^3}} \quad (33)$$

Combining (31) and (33), $|b|$ is bounded by

$$\begin{aligned} |b| &\leq \frac{\pi\lambda}{4} \frac{1}{0.62} \sqrt{\frac{\lambda}{D^3}} \\ &= \frac{\pi}{4 \times 0.62} \sqrt{\frac{\lambda^3}{D^3}} \\ &\stackrel{(a)}{=} \frac{\pi}{4 \times 0.62} \sqrt{\frac{\lambda^3}{(N-1)^3 d^3}} \\ &\stackrel{(b)}{<} \frac{\pi}{1.24(N-1)} \sqrt{\frac{2}{N-1}} \stackrel{(c)}{<} \pi \end{aligned} \quad (34)$$

where (a) is due to $D = (N-1)d$, (b) follows from $d = \lambda/2$, and (c) holds true when $N > 2$.

Define \tilde{a} as

$$\tilde{a} \triangleq \text{mod}(a + \pi, 2\pi) - \pi \quad (35)$$

It is clear that $\tilde{a} \in [-\pi, \pi]$. Meanwhile, we have

$$e^{-jan} = e^{-j\tilde{a}n} \quad (36)$$

due to the fact that $n \in \{0, \dots, N-1\}$. Therefore, we have the following result:

$$\begin{aligned} S(a, b) &= \frac{1}{N} \sum_{n=0}^{N-1} e^{-jan} e^{-jbn^2} \\ &= \frac{1}{N} \sum_{n=0}^{N-1} e^{-j\tilde{a}n} e^{-jbn^2} \triangleq S(\tilde{a}, b) \end{aligned} \quad (37)$$

In addition, $S(\tilde{a}, b)$ can be approximated as

$$\begin{aligned} S(\tilde{a}, b) &= \frac{1}{N} \sum_{n=0}^{N-1} e^{-j\tilde{a}n} e^{-jbn^2} \\ &\stackrel{(a)}{\approx} \frac{1}{N} \int_{n=0}^{N-1} e^{-j\tilde{a}n} e^{-jbn^2} dn \\ &\stackrel{(b)}{=} \frac{1}{N} \int_{n=0}^{N-1} e^{-j(\sqrt{bn} + \frac{\tilde{a}}{2\sqrt{b}})^2 - j\frac{\tilde{a}^2}{4b}} dn \\ &= \frac{1}{N} e^{-j\frac{\tilde{a}^2}{4b}} \int_{n=0}^{N-1} e^{-j(\sqrt{bn} + \frac{\tilde{a}}{2\sqrt{b}})^2} dn \\ &= \frac{1}{N} \frac{e^{-j\frac{\tilde{a}^2}{4b}}}{\sqrt{b}} \int_{n=\frac{\tilde{a}}{2\sqrt{b}}}^{(N-1)\sqrt{b} + \frac{\tilde{a}}{2\sqrt{b}}} e^{-jn^2} dn \\ &= \frac{1}{N} \frac{e^{-j\frac{\tilde{a}^2}{4b}}}{\sqrt{b}} (f_1(a, b) - jf_2(a, b)) \end{aligned} \quad (38)$$

where in (a), the summation is approximated by an integral [30], and (b) is due to the assumption $b > 0$, $f_1(a, b)$ and $f_2(a, b)$ are, respectively, defined in (25) and (26).

Combining (21), (37) and (38), we have

$$|f(a, b)| \approx \frac{1}{N\sqrt{|b|}} \sqrt{|f_1(a, b)|^2 + |f_2(a, b)|^2} \quad (39)$$

Thus we obtain the expression of $|f(a, b)|$ for the case $b > 0$.

When $b < 0$, the expression in (39) still holds true, except that the Fresnel integral should be generalized to the complex domain. Specifically, for the case $b < 0$, $S(\tilde{a}, b)$ can be expressed by

$$\begin{aligned} S(\tilde{a}, b) &= \frac{1}{N} \sum_{n=0}^{N-1} e^{-j\tilde{a}n} e^{-jbn^2} \\ &\approx \frac{1}{N} \int_{n=0}^{N-1} e^{-j\tilde{a}n} e^{j|b|n^2} dn \\ &= \frac{1}{N} \int_{n=0}^{N-1} e^{j(\sqrt{|b|n} - \frac{\tilde{a}}{2\sqrt{|b|}})^2 - j\frac{\tilde{a}^2}{4|b|}} dn \\ &= \frac{1}{N} e^{-j\frac{\tilde{a}^2}{4|b|}} \int_{n=0}^{N-1} e^{j(\sqrt{|b|n} - \frac{\tilde{a}}{2\sqrt{|b|}})^2} dn \\ &= \frac{e^{-j\frac{\tilde{a}^2}{4|b|}}}{N\sqrt{|b|}} \int_{n=-\frac{\tilde{a}}{2\sqrt{|b|}}}^{(N-1)\sqrt{|b|} - \frac{\tilde{a}}{2\sqrt{|b|}}} e^{jn^2} dn \\ &= \frac{e^{-j\frac{\tilde{a}^2}{4|b|}}}{N\sqrt{|b|}} (f_3(a, b) + jf_4(a, b)) \end{aligned} \quad (40)$$

where $f_3(a, b)$ and $f_4(a, b)$ are, respectively, given by

$$\begin{aligned} f_3(a, b) &\triangleq C \left((N-1)\sqrt{|b|} - \frac{\tilde{a}}{2\sqrt{|b|}} \right) - C \left(-\frac{\tilde{a}}{2\sqrt{|b|}} \right) \\ f_4(a, b) &\triangleq S \left((N-1)\sqrt{|b|} - \frac{\tilde{a}}{2\sqrt{|b|}} \right) - S \left(-\frac{\tilde{a}}{2\sqrt{|b|}} \right) \end{aligned}$$

Furthermore, since we have $|b| = -b$ when $b < 0$, $f_3(a, b)$ can be rewritten as

$$\begin{aligned} f_3(a, b) &= C \left(j(N-1)\sqrt{b} - \frac{\tilde{a}}{2j\sqrt{b}} \right) - C \left(-\frac{\tilde{a}}{2j\sqrt{b}} \right) \\ &\stackrel{(a)}{=} j \left(C \left((N-1)\sqrt{b} + \frac{\tilde{a}}{2\sqrt{b}} \right) - C \left(\frac{\tilde{a}}{2\sqrt{b}} \right) \right) \\ &= jf_1(a, b) \end{aligned} \quad (41)$$

where in (a) we utilized the identity $C(j\zeta) = jC(\zeta)$ [31]. Similarly, by using $S(j\zeta) = -jS(\zeta)$ [31], $f_4(a, b)$ can be expressed as

$$f_4(a, b) = -jf_2(a, b) \quad (42)$$

Therefore, when $b < 0$, $S(\tilde{a}, b)$ can be written as

$$S(\tilde{a}, b) = \frac{e^{-j\frac{\tilde{a}^2}{4|b|}}}{N\sqrt{|b|}} (jf_1(a, b) + f_2(a, b)) \quad (43)$$

Thus the expression of $|f(a, b)|$ is the same as (39). This completes our proof. \blacksquare

V. MAIN RESULTS

Based on the above analysis, we now determine the condition under which $|f(a, b)|$ is sufficiently small to be considered approximately zero. Intuitively, $|f(a, b)|$ (equivalent to $|\alpha_0(m)|$) tends to zero when $\{\sin(\theta_m), \sin(\theta_0)\}$ or $\{r_0, r_p\}$ are sufficiently separated. In this section, we will theoretically analyze how far should two angles (i.e., $\sin(\theta_m)$ and $\sin(\theta_0)$) be separated to ensure $|f(a, b)|$ is no greater than a given small positive threshold δ .

A. The Case of $b = 0$

When $b = 0$, we have

$$|f(a, b)| = \frac{1}{N} \left| \frac{1 - e^{-jNa}}{1 - e^{-ja}} \right| \leq \frac{2}{N} \left| \frac{1}{1 - e^{-ja}} \right| \quad (44)$$

To make sure $|f(a, b)| < \delta$, we need

$$\frac{2}{N} \left| \frac{1}{1 - e^{-ja}} \right| < \delta \quad (45)$$

which gives

$$|1 - e^{-ja}| = \sqrt{2 - 2\cos(a)} > \frac{2}{N\delta} \quad (46)$$

It should be noted that $|1 - e^{-ja}|$ is no greater than 2. Therefore, in (46), we implicitly assume that $2/(N\delta) < 2$, which implies $\delta > 1/N$. Therefore, we have

$$\cos(a) < 1 - \frac{2}{N^2\delta^2} \quad (47)$$

which indicates that a sufficient condition to ensure $|f(a, b)| < \delta$ is given as

$$\arccos\left(1 - \frac{2}{N^2\delta^2}\right) < |\tilde{a}| \leq \pi \quad (48)$$

where $\tilde{a} \triangleq \text{mod}(a + \pi, 2\pi) - \pi$ is defined in (27). Based on the relation between sufficient and necessary conditions, we have the following result:

Theorem 1: When $r_p = r_0$, a necessary condition for

$$|f(a, b)| \geq \delta \quad (49)$$

is that

$$|\tilde{a}| \leq \arccos\left(1 - \frac{2}{N^2\delta^2}\right) \quad (50)$$

According to the definition of \tilde{a} , we can rewrite the result in Theorem 1 as

$$\left| \text{mod}\left(\frac{2\pi d}{\lambda} (\sin(\theta_m) - \sin(\theta_0)) + \pi, 2\pi\right) - \pi \right| \leq \arccos\left(1 - \frac{2}{N^2\delta^2}\right) \quad (51)$$

Note that $\lambda = 2d$ and

$$ka \equiv \text{mod}(kb, kc) \Leftrightarrow a \equiv \text{mod}(b, c) \text{ if } k \neq 0$$

We can rewrite (51) as

$$\left| \text{mod}((\sin(\theta_m) - \sin(\theta_0)) + 1, 2) - 1 \right| \leq \eta_0 \quad (52)$$

in which η_0 is defined as

$$\eta_0 \triangleq \frac{1}{\pi} \arccos\left(1 - \frac{2}{N^2\delta^2}\right) \quad (53)$$

B. The Case of $b > 0$

1) When $\tilde{a} > 0$: Before discussing the case where $b > 0$ and $\tilde{a} > 0$, we first introduce the following proposition:

Proposition 3: If $x > 0$ and $\Delta > 0$, then the following inequalities hold:

$$|C(x + \Delta) - C(x)| < \frac{1}{x} \quad (54)$$

$$|S(x + \Delta) - S(x)| < \frac{1}{x} \quad (55)$$

Proof: See Appendix A. ■

Applying Proposition 3 to $f_1(a, b)$ and $f_2(a, b)$, we have

$$|f_1(a, b)| < \frac{2\sqrt{b}}{\tilde{a}}, \quad |f_2(a, b)| < \frac{2\sqrt{b}}{\tilde{a}} \quad (56)$$

As a result, we have

$$|f(a, b)| = \frac{1}{N\sqrt{b}} \sqrt{f_1^2(a, b) + f_2^2(a, b)} < \frac{2\sqrt{2}}{N\tilde{a}} \quad (57)$$

To ensure $|f(a, b)| < \delta$, the following inequality should be satisfied

$$\frac{2\sqrt{2}}{N\tilde{a}} < \delta \quad (58)$$

which leads to

$$\frac{2\sqrt{2}}{N\delta} < \tilde{a} \leq \pi \quad (59)$$

Note that in (59) we implicitly assume that

$$\frac{2\sqrt{2}}{N\delta} < \pi$$

which is equivalent to

$$\delta > \frac{2\sqrt{2}}{N\pi} \approx \frac{0.9}{N} \quad (60)$$

The above condition can be met for a sufficiently large N .

2) When $\tilde{a} < 0$: The case with $b > 0$ and $\tilde{a} < 0$ is much more complex since we cannot directly utilize Proposition 3. To deal with this challenge, we apply the following properties of the Fresnel integrals, i.e., $C(-\zeta) = -C(\zeta)$ and $S(-\zeta) = -S(\zeta)$, and rewrite $f_1(a, b)$ and $f_2(a, b)$ as follows

$$f_1(a, b) \triangleq C\left(\frac{-\tilde{a}}{2\sqrt{b}}\right) - C\left(\frac{-\tilde{a}}{2\sqrt{b}} - (N-1)\sqrt{b}\right) \quad (61)$$

$$f_2(a, b) \triangleq S\left(\frac{-\tilde{a}}{2\sqrt{b}}\right) - S\left(\frac{-\tilde{a}}{2\sqrt{b}} - (N-1)\sqrt{b}\right) \quad (62)$$

If $-\tilde{a}/(2\sqrt{b}) - (N-1)\sqrt{b} > 0$, we have, according to Proposition 3,

$$|f_1(a, b)| < \frac{1}{-\frac{\tilde{a}}{2\sqrt{b}} - (N-1)\sqrt{b}} \quad (63)$$

$$|f_2(a, b)| < \frac{1}{-\frac{\tilde{a}}{2\sqrt{b}} - (N-1)\sqrt{b}} \quad (64)$$

which gives

$$|f(a, b)| < \frac{\sqrt{2}}{N\sqrt{b}} \frac{1}{-\frac{\tilde{a}}{2\sqrt{b}} - (N-1)\sqrt{b}} \quad (65)$$

Let

$$\frac{\sqrt{2}}{N\sqrt{b}} \frac{1}{-\frac{\tilde{a}}{2\sqrt{b}} - (N-1)\sqrt{b}} < \delta \quad (66)$$

We have

$$-\pi \leq \tilde{a} < -\left(\frac{2\sqrt{2}}{N\delta} + 2(N-1)b\right) \quad (67)$$

On the other hand, when $-\tilde{a}/(2\sqrt{b}) - (N-1)\sqrt{b} \leq 0$, we have

$$f_1(a, b) = C\left(\frac{-\tilde{a}}{2\sqrt{b}}\right) + C\left(\frac{\tilde{a}}{2\sqrt{b}} + (N-1)\sqrt{b}\right) \quad (68)$$

$$f_2(a, b) = S\left(\frac{-\tilde{a}}{2\sqrt{b}}\right) + S\left(\frac{\tilde{a}}{2\sqrt{b}} + (N-1)\sqrt{b}\right) \quad (69)$$

Based on the fact $C(\zeta) < 0.98$ and $S(\zeta) < 0.90$ for $\zeta > 0$ (the validness of the results can be numerically verified), we can arrive at

$$|f(a, b)| = \frac{1}{N\sqrt{b}} \sqrt{f_1^2(a, b) + f_2^2(a, b)} < \frac{2.7}{N\sqrt{b}} \quad (70)$$

Thus, we can let

$$\sqrt{b} > \frac{2.7}{N\delta} \quad (71)$$

to ensure $|f(a, b)| < \delta$. Meanwhile, from (34) we know that

$$b \leq \frac{\pi}{1.24(N-1)} \sqrt{\frac{2}{N-1}} \quad (72)$$

To guarantee (71) and (72) hold simultaneously, the following condition should be satisfied

$$\frac{(N\delta)^2}{(N-1)\sqrt{N-1}} > 2.035 \quad (73)$$

Nevertheless, for a large value of N and a small positive δ , the above condition does not hold valid. Therefore, we can draw a conclusion that when $-\tilde{a}/(2\sqrt{b}) - (N-1)\sqrt{b} \leq 0$, there is no way to ensure $|f(a, b)|$ is smaller than δ .

Based on the above analysis, we can conclude that when $b > 0$, \tilde{a} needs to satisfy the following condition in order to guarantee $|f(a, b)| < \delta$:

$$-\pi \leq \tilde{a} < -\left(\frac{2\sqrt{2}}{N\delta} + 2(N-1)b\right) \text{ or } \frac{2\sqrt{2}}{N\delta} < \tilde{a} \leq \pi \quad (74)$$

According to the relation between sufficient conditions and necessary conditions, we also have the following proposition:

Theorem 2: When $r_p > r_0$, a necessary condition for

$$|f(a, b)| \geq \delta \quad (75)$$

is that

$$-\left(\frac{2\sqrt{2}}{N\delta} + 2(N-1)b\right) \leq \tilde{a} \leq \frac{2\sqrt{2}}{N\delta} \quad (76)$$

Similar to (52), (76) can be converted to

$$-\eta_2 \leq \text{mod}((\sin(\theta_m) - \sin(\theta_0)) + 1, 2) - 1 \leq \eta_1 \quad (77)$$

where η_1 and η_2 are, respectively, defined as

$$\eta_1 \triangleq \frac{2\sqrt{2}}{N\pi\delta} \quad (78)$$

$$\begin{aligned} \eta_2 &\triangleq \left(\frac{2\sqrt{2}}{N\pi\delta} + \frac{2(N-1)|b|}{\pi}\right) \\ &\stackrel{(a)}{=} \left(\frac{2\sqrt{2}}{N\pi\delta} + D\left|\frac{1}{r_0} - \frac{1}{r_p}\right|\right) \end{aligned} \quad (79)$$

where in (a) we utilized the definition of b .

C. The Case Of $b < 0$

In the following we discuss the case where $b < 0$, i.e., $r_p < r_0$. First of all, we have the following proposition:

Proposition 4: When $b < 0$, the following relationship holds:

$$|f(a, b)| = |f(-a, -b)| \quad (80)$$

Proof: Apparently, $f(a, b)$ is determined by $f_1(a, b)$ and $f_2(a, b)$. We first consider $f_1(a, b)$. From (25), we have

$$\begin{aligned} f_1(a, b) &\triangleq C\left((N-1)\sqrt{b} + \frac{\tilde{a}}{2\sqrt{b}}\right) - C\left(\frac{\tilde{a}}{2\sqrt{b}}\right) \\ &= C\left(j(N-1)\sqrt{-b} + j\frac{-\tilde{a}}{2\sqrt{-b}}\right) - C\left(j\frac{-\tilde{a}}{2\sqrt{-b}}\right) \\ &= j\left(C\left((N-1)\sqrt{-b} + \frac{-\tilde{a}}{2\sqrt{-b}}\right) - C\left(\frac{-\tilde{a}}{2\sqrt{-b}}\right)\right) \\ &\stackrel{(a)}{=} jf_1(-a, -b) \end{aligned} \quad (81)$$

where in (a) we utilized the following property

$$-\tilde{a} \triangleq -\text{mod}(a + \pi, 2\pi) + \pi \equiv \text{mod}(-a + \pi, 2\pi) - \pi \quad (82)$$

which holds true when $|a| \neq \pi$. Similarly, for $f_2(a, b)$ in (26) we have

$$\begin{aligned} f_2(a, b) &\triangleq S\left((N-1)\sqrt{b} + \frac{\tilde{a}}{2\sqrt{b}}\right) - S\left(\frac{\tilde{a}}{2\sqrt{b}}\right) \\ &= S\left(j(N-1)\sqrt{b} + j\frac{-\tilde{a}}{2\sqrt{b}}\right) - S\left(j\frac{-\tilde{a}}{2\sqrt{b}}\right) \\ &= -j\left(S\left((N-1)\sqrt{b} + \frac{-\tilde{a}}{2\sqrt{b}}\right) - S\left(\frac{-\tilde{a}}{2\sqrt{b}}\right)\right) \\ &\stackrel{(a)}{=} -jf_2(-a, -b) \end{aligned} \quad (83)$$

where (a) is due to (82). Therefore, when $|a| \neq \pi$, we have

$$\begin{aligned} |f(a, b)| &= \frac{1}{N} \left| \frac{1}{\sqrt{b}} (f_1(a, b) - jf_2(a, b)) \right| \\ &= \frac{1}{N} \left| \frac{1}{j\sqrt{-b}} (jf_1(-a, -b) - f_2(-a, -b)) \right| \\ &= \frac{1}{N\sqrt{|b|}} \left| \sqrt{|f_1(-a, -b)|^2 + |f_2(-a, -b)|^2} \right| \\ &= |f(-a, -b)| \end{aligned} \quad (84)$$

which establishes (80) for $|a| \neq \pi$.

In the following, we discuss the case when $|a| = \pi$. Under such a circumstance, it can be verified that

$$\begin{aligned} S(a, b) &= \sum_{n=0}^{N-1} e^{\pm j\pi n} e^{-jbn^2} = \sum_{n=0}^{N-1} e^{-jbn^2} \\ &\approx \frac{1}{\sqrt{|b|}} \left(C \left((N-1)\sqrt{|b|} \right) + jS \left((N-1)\sqrt{|b|} \right) \right) \\ &\stackrel{(a)}{=} \frac{1}{\sqrt{|b|}} (f_3(0, b) + jf_4(0, b)) \\ &\stackrel{(b)}{=} \frac{1}{\sqrt{|b|}} (jf_1(0, b) + f_2(0, b)) \end{aligned} \quad (85)$$

where (a) follows from (40) and (b) is due to (41) and (42). Therefore, $|f(a, b)|$ can be obtained as

$$\begin{aligned} |f(a, b)| &= \frac{1}{N\sqrt{|b|}} |f_2(0, b) + jf_1(0, b)| \\ &= |f(0, b)| \\ &= \frac{1}{N\sqrt{|b|}} |-jf_2(0, -b) - f_1^2(0, -b)| \\ &= \frac{1}{N\sqrt{|b|}} \sqrt{|f_1(0, -b)|^2 + |f_2(0, -b)|^2} \\ &= |f(0, -b)| \end{aligned} \quad (86)$$

which indicates that

$$|f(\pm\pi, b)| = |f(0, b)| = |f(0, -b)| \quad (87)$$

which establishes (80) for $|a| = \pi$. This completes the proof. \blacksquare

Utilizing Theorem 2 and Proposition 4, we can arrive at the following result:

Theorem 3: When $r_p < r_0$, a necessary condition for

$$|f(a, b)| \geq \delta \quad (88)$$

is that

$$-\frac{2\sqrt{2}}{N\delta} \leq \tilde{a} \leq \frac{2\sqrt{2}}{N\delta} + 2(N-1)|b| \quad (89)$$

The condition (89) is equivalent to

$$-\eta_1 \leq \text{mod}((\sin(\theta_m) - \sin(\theta_0)) + 1, 2) - 1 \leq \eta_2 \quad (90)$$

where the definition of η_1 and η_2 are, respectively, given by (78) and (79).

D. Summary

In the above, we have derived the condition that the value of \tilde{a} (i.e., $\sin(\theta_m) - \sin(\theta_0)$) should be satisfied (i.e., (52), (77) and (90)) to ensure $|f(a, b)|$ (or equivalently the m th element of α_0) is greater than a given threshold δ . If we treat an entry less than δ as a zero entry and an entry no less than δ as a non-zero entry, the indices of non-zero entries in α_0 can be obtained by checking the related inequalities in (52), (77) or (90). Take the case of $b > 0$ as an example. Considering the fact $\sin(\theta_m), \sin(\theta_0) \in [-1, 1]$, the inequality (77) can be translated into the following different cases. When $\sin(\theta_0) + \eta_1 \leq 1$ and $\sin(\theta_0) - \eta_2 \geq -1$, (77) becomes

$$\left\{ m \mid \sin(\theta_0) - \eta_2 \leq \sin(\theta_m) \leq \sin(\theta_0) + \eta_1 \right\} \quad (91)$$

When $\sin(\theta_0) + \eta_1 > 1$, (77) becomes

$$\left\{ m \mid \begin{array}{l} \sin(\theta_0) - \eta_2 \leq \sin(\theta_m) \leq 1, \\ -1 \leq \sin(\theta_m) \leq -2 + \sin(\theta_0) + \eta_1 \end{array} \right\} \quad (92)$$

When $\sin(\theta_0) - \eta_2 < -1$, (77) becomes

$$\left\{ m \mid \begin{array}{l} 2 + \sin(\theta_0) - \eta_2 \leq \sin(\theta_m) \leq 1, \\ -1 \leq \sin(\theta_m) \leq \sin(\theta_0) + \eta_1 \end{array} \right\} \quad (93)$$

From (91), (92) and (93), we can see that the indices of the non-zero elements in α_0 has a clustered pattern, i.e., these non-zero entries either are located around $\sin(\theta_0)$ (i.e., (91)) or located around the two sides of the interval $[-1, 1]$ (i.e., (92) or (93)).

We also would like to derive the total number of non-zeros elements in α_0 , i.e., the cardinality of the set $\{m \mid \alpha_0(m) \geq \delta\}$, which is denoted as \bar{K} . From the above analysis, it can be easily verified that to ensure $\alpha_0(m) \geq \delta$, the interval width for $\sin(\theta_m)$ is given by

$$\Omega = \begin{cases} 2\eta_0, & b = 0 \\ \eta_1 + \eta_2, & b \neq 0 \end{cases} \quad (94)$$

Note that the angular resolution of a ULA with N antennas is $2/N$, i.e., $\sin(\theta_{m+1}) - \sin(\theta_m) = 2/N$ for $m = 1, \dots, N-1$. Therefore, \bar{K} , the cardinality of the set $\{m \mid \alpha_0(m) \geq \delta\}$ can be obtained as

$$\bar{K} = \left\lceil \frac{\Omega}{2/N} \right\rceil \quad (95)$$

which can be further simplified as

$$\bar{K} = \begin{cases} \lceil \eta_0 N \rceil & b = 0 \\ \left\lceil \frac{(\eta_1 + \eta_2)N}{2} \right\rceil & b \neq 0 \end{cases} \quad (96)$$

where $\lceil \cdot \rceil$ denotes the ceiling function.

When $b = 0$, \bar{K} is given as

$$\bar{K} = \left\lceil \frac{N}{\pi} \arccos \left(1 - \frac{2}{N^2 \delta^2} \right) \right\rceil \quad (97)$$

When N tends to ∞ , $2/(N^2 \delta^2)$ tends to 0. It is known that the Puiseux series of $\arccos(1-x)$ around $x = 0^+$ is given as

$$\arccos(1-x) = \sqrt{2x} + \frac{(2x)^{3/2}}{24} + \mathcal{O}(x^{5/2}) \quad (98)$$

Therefore, we have

$$\lim_{N \rightarrow \infty} \frac{N}{\pi} \arccos \left(1 - \frac{2}{N^2 \delta^2} \right) = \frac{2}{\pi \delta} \quad (99)$$

which leads to

$$\lim_{N \rightarrow \infty} \bar{K} = \left\lceil \frac{2}{\pi \delta} \right\rceil \quad (100)$$

We see that when $b = 0$, the number of nonzero entries in α_0 , \bar{K} , tends to be a constant as N goes to infinity.

When $b \neq 0$, \bar{K} is given by

$$\bar{K} = \left\lceil \frac{2\sqrt{2}}{\pi \delta} + \frac{ND}{2} \left| \frac{1}{r_0} - \frac{1}{r_p} \right| \right\rceil \quad (101)$$

From (33) we know that

$$\left| \frac{1}{r_0} - \frac{1}{r_p} \right| \leq \frac{1}{0.62} \sqrt{\frac{\lambda}{D^3}} \quad (102)$$

Therefore, we have

$$\frac{ND}{2} \left| \frac{1}{r_0} - \frac{1}{r_p} \right| \leq \frac{N}{1.24} \sqrt{\frac{2}{N-1}} \quad (103)$$

We see that when $b \neq 0$, the number of nonzero entries in α_0 , \bar{K} , increases sublinearly in N , i.e. $\bar{K} \sim \sqrt{N}$. Hence the percentage of nonzero entries in α_0 is at the order of $1/\sqrt{N}$, which tends to a small value as N becomes sufficiently large. Since the non-zero elements of α_0 has a clustered pattern, we can conclude that α_0 has a block-sparse structure.

Remark 1: From (101), we can see that the number of non-zero elements \bar{K} decreases when r_p gets closer to r_0 . Therefore, when devising the dictionary \mathbf{D}_{r_p} , one should let r_p be as close to r_0 as possible such that a sparser representation of the near-field channel can be obtained. In real applications, the knowledge of r_0 may be roughly estimated from the location information of the user. Even if this knowledge is unavailable, our results reveal that for an arbitrary choice of r_p (as long as it lies in the radiative zone), the near-field channel would have a desirable block-sparse representation on the dictionary \mathbf{D}_{r_p} when the number of antennas at the BS is sufficiently large.

VI. CHANNEL ESTIMATION AND RIP CONDITION ANALYSIS

A. Channel Estimation

From the above analysis, we know that the hybrid near/far-field channel admits a block-sparse representation on a dictionary \mathbf{D}_{r_p} , i.e., $\mathbf{h} = \mathbf{D}_{r_p} \alpha_{r_p}$. Substituting this sparse representation into the received signal model (2) results in

$$\mathbf{y} = \mathbf{F} \mathbf{D}_{r_p} \alpha_{r_p} + \mathbf{n} \triangleq \mathbf{\Psi} \alpha_{r_p} + \mathbf{n} \quad (104)$$

where $\mathbf{\Psi} \triangleq \mathbf{F} \mathbf{D}_{r_p}$ is the sensing matrix. Note that elements of \mathbf{F} can be randomly selected from $\{+1/\sqrt{N}, -1/\sqrt{N}\}$ with equal probability or i.i.d. random variables following a complex Gaussian distribution $\mathcal{CN}(0, 1/N)$.

Based on (104), the hybrid near/far-field channel estimation problem can be converted into a block-sparse signal recovery problem whose objective is to recover a block-sparse α_{r_p} from noise-corrupted observations \mathbf{y} . Many classical block-sparse signal recovery algorithms such as CoSaMP [32] and the block-OMP [33] can be applied to solve our hybrid near/far-field channel estimation problem. Note that the CoSaMP and block-OMP methods require the knowledge of block-partition. For our considered problem, both the locations of non-zero elements and the size of the nonzero block depend on some unknown parameters such as $\sin(\theta_0)$. As a result, the block partition of the block-sparse signal is usually unavailable. In this case, the CoSaMP and block-OMP methods may incur a potential performance loss. Instead, some other block-sparse signal recovery algorithms such as the pattern-coupled sparse Bayesian learning [34] that do not need the knowledge of block partition can be employed obtain a more accurate estimate of the hybrid near/far-field channel.

B. Block-RIP Condition

In the following, we provide an analysis to show how many measurements are required to enable a reliable recovery of the high-dimensional hybrid near/far channel vector. To answer this question, we introduce the notion of block RIP which is an extension of the RIP to a block-sparse vector. We first provide the definition of a block k -sparse signal as follows:

Definition 1 ([35]): Consider a vector $\mathbf{c} \in \mathbb{C}^N$ that can be divided sequentially into M non-overlapping blocks, i.e.,

$$\mathbf{c} = [\mathbf{c}_1^H \ \cdots \ \mathbf{c}_i^H \ \cdots \ \mathbf{c}_M^H]^H \quad (105)$$

where \mathbf{c}_i is the i th block of length d_i with $N = \sum_{i=1}^M d_i$. Define the set $\mathcal{I} = \{d_1, \dots, d_M\}$. \mathbf{c} is called block k -sparse over \mathcal{I} if

$$\|\mathbf{c}\|_{0,\mathcal{I}} = \sum_{i=1}^M \mathbb{I}(\|\mathbf{c}_i\|_2 > 0) \leq k \quad (106)$$

where $\mathbb{I}(\|\mathbf{c}_i\|_2 > 0)$ is an indicator function:

$$\mathbb{I}(\|\mathbf{c}_i\|_2 > 0) = \begin{cases} 1, & \|\mathbf{c}_i\|_2 > 0 \\ 0, & \text{otherwise} \end{cases} \quad (107)$$

With the definition of block k -sparse, the block RIP is defined as:

Definition 2 ([35]): Consider a given matrix $\mathbf{D} \in \mathbb{C}^{n \times N}$. Then \mathbf{D} has the block RIP over the set $\mathcal{I} \triangleq \{d_1, \dots, d_M\}$ with parameter $\xi_{k,\mathcal{I}}$ if for arbitrary $\mathbf{c} \in \mathbb{C}^N$ that is block k -sparse over \mathcal{I} we have that

$$(1 - \xi_{k,\mathcal{I}}) \|\mathbf{c}\|_2^2 \leq \|\mathbf{D}\mathbf{c}\|_2^2 \leq (1 + \xi_{k,\mathcal{I}}) \|\mathbf{c}\|_2^2 \quad (108)$$

From our previous analysis, we know that the size of the nonzero block in α_{r_p} is in the order of \sqrt{N} . Therefore we uniformly divide the N entries of α_{r_p} into \sqrt{N} blocks, where we assume \sqrt{N} is an integer number. Under such a circumstance, the set \mathcal{I} is written as

$$\mathcal{I} = \{d_1, \dots, d_M\} \quad (109)$$

with $M = \sqrt{N}$ and $d_i = \sqrt{N}$, $\forall i \in \{1, \dots, M\}$. According to our previous analysis, we can conclude that α_{r_p} is block ϱ -sparse over the set \mathcal{I} , with ϱ given as

$$\begin{aligned} \varrho &= \left\lceil \frac{\bar{K}}{\sqrt{N}} \right\rceil \\ &\stackrel{(a)}{\leq} \left\lceil \frac{2\sqrt{2}}{\pi\delta\sqrt{N}} + \frac{ND}{2\sqrt{N}} \left| \frac{1}{r_0} - \frac{1}{r_p} \right| \right\rceil \\ &\stackrel{(b)}{\leq} \left\lceil \frac{2\sqrt{2}}{\pi\delta\sqrt{N}} + \frac{\sqrt{2}}{1.24} \sqrt{\frac{N}{N-1}} \right\rceil \end{aligned} \quad (110)$$

where in (a) we used the largest possible number of non-zero elements in α_{r_p} and meanwhile utilized the fact that $\lceil \lceil a \rceil \rceil \equiv \lceil a \rceil$, and in (b) we applied the inequality in (103). It can be readily verified that, when setting $\delta = 0.01$ and $N \geq 256$, ϱ is no greater than 7.

For the block ϱ -sparse signal α_{r_p} , we have the following theorem:

Theorem 4: Let $\kappa > 0$ and $0 < \xi < 1$ be constant numbers. If

$$T \geq \frac{36}{7\xi} \left(\varrho \ln \left(\frac{e\sqrt{N}}{\varrho} \right) + \varrho\sqrt{N} \ln \left(\frac{12}{\xi} \right) + \ln 2 + \kappa \right) \quad (111)$$

then Ψ satisfies the block-RIP defined in (108) with $\xi_{\varrho, \mathcal{I}} = \xi$ with probability at least $1 - e^{-\kappa}$.

Proof: See Appendix B. ■

According to Theorem 4, since ϱ is generally smaller than \sqrt{N} , roughly $\mathcal{O}(\sqrt{N})$ observations are required to guarantee the block-RIP of Ψ . In contrast, if the block-sparse structure is ignored, the observations should be on the order of $\mathcal{O}(\sqrt{N} \ln(N))$ to ensure Ψ satisfies the standard RIP condition. Since $\sqrt{N} \ll N$ for a large value of N , this means that our proposed method can achieve a substantial training overhead reduction. On the other hand, we would like to point out that the above analysis is pessimistic as it applies for an arbitrary dictionary D_{r_p} . When the dictionary D_{r_p} is carefully chosen such that r_p is close to r_0 , from (100) we see that \bar{K} would approach a constant, which means that the number of nonzero entries in α_{r_p} remains a constant that is independent of N . As a result, the number of measurements required to recover the channel would be much fewer than predicted by Theorem 4.

VII. NUMERICAL SIMULATIONS

In this section, simulation results are presented to verify our theoretical results and illustrate the channel estimation performance of the proposed method.

A. Theoretical Result

First, we evaluate the analytical results concerning the coherence of two near-field steering vectors, i.e., results in Proposition 2. We consider a BS with N antennas operating at 100GHz, where N varies from 256 to 2560. The spatial angles of the two near-field steering vectors are randomly selected from the interval $[-1, 1]$, and the associated distance parameters are randomly sampled from the interval $[Z_1, Z_2]$. We implement 1000 Monte Carlo runs for each N to calculate the error between the analytical result (24) and the simulation result, which is illustrated in Fig. 2. It can be seen that, when setting N to 256, the approximation error of our derived analytical result is smaller than 10^{-2} , and such an approximation error decreases gradually with the increase of N . Therefore, it can be concluded that the approximation accuracy of the analytical result (24) is sufficiently accurate for our theoretical analysis.

Next, we evaluate the sparsity level of α_0 versus N . The sparsity level refers to the percentage of non-zero elements in α_0 . The theoretical bound of the sparsity level is obtained by \bar{K}/N , where \bar{K} is shown in (101) and δ is set to 0.01. In such a setup, the element in α_0 with its magnitude below 0.01 is considered as a zero element. The sparsity level is obtained by averaging results of 1000 independent Monte Carlo runs. For each Monte Carlo run, α_0 is obtained via $D_{r_p}^H \mathbf{a}(\theta_0, r_0)$, where the parameters $\{r_p, r_0, \theta_0\}$ are randomly

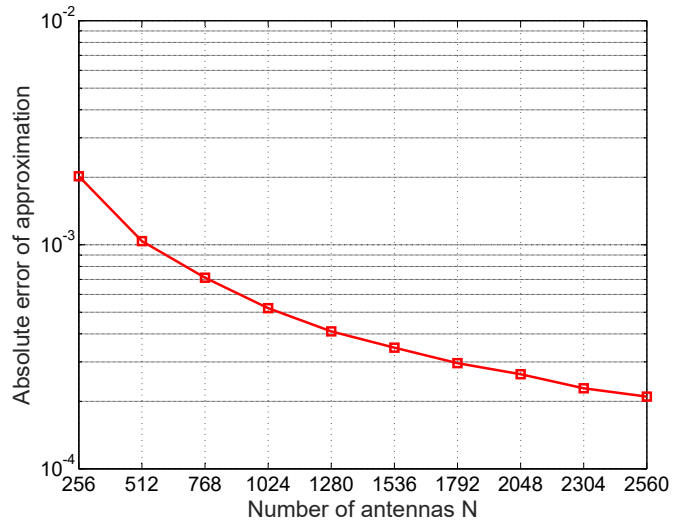


Fig. 2: The absolute approximation error for the coherence of two near-filed steering vector versus N

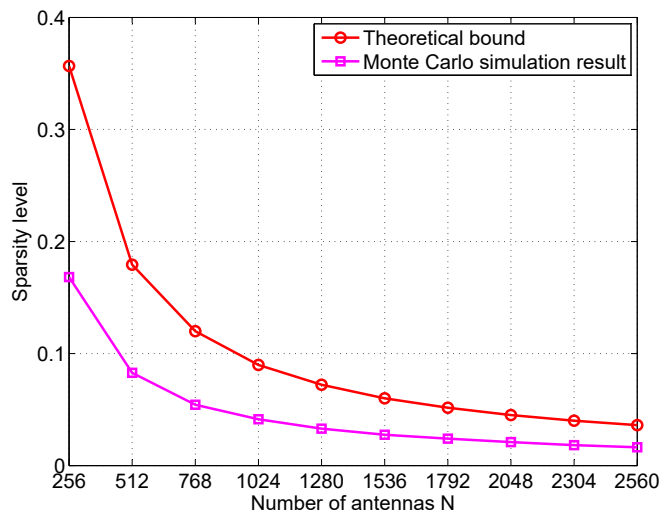


Fig. 3: The sparsity level of α_{r_p} versus N

generated in a same way as above. Fig. 3 depicts the theoretical and numerical sparsity level results. It can be seen that our theoretical result provides a loose upper bound on the true sparsity level of α_0 . In addition, when N grows, the sparsity level decreases accordingly. Particularly, when N is larger than 512, the sparsity level drops below 0.2. Therefore, α_0 is indeed a sparse vector, especially for scenarios with a large N .

B. Channel Estimation Result

We now present results to illustrate the performance of the proposed block-sparsity-aware channel estimation method. We compare our method with the polar-domain based on-grid and off-grid near-field channel estimation algorithms [19]. In [19], the orthogonal matching pursuit (OMP) method is employed

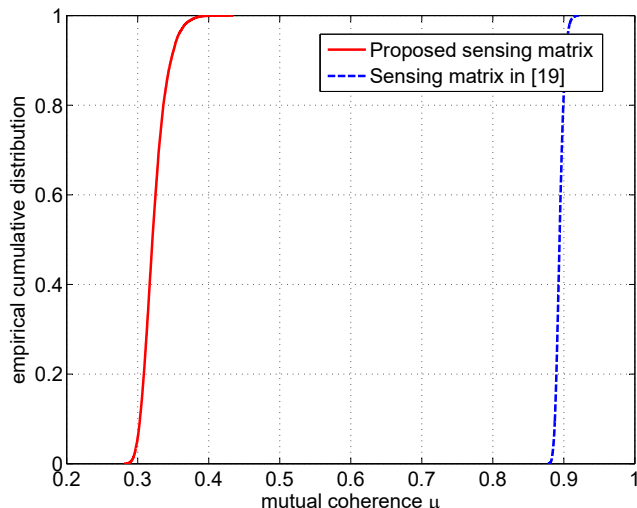


Fig. 4: The mutual coherence of two different sensing matrices

to recover the sparse channel. For a fair comparison, here we employ a block-OMP method [33] to solve our formulated compressed sensing problem.

We consider a communication system operating at 100GHz with a BS equipped with $N = 256$ antennas. We assume that there are $L = 3$ propagation paths including a LOS path and two NLOS paths. The ratio of the signal power of the LOS path to the power of the NLOS paths is set to 13dB [36]. The angle and the distance parameters of each path are, respectively, uniformly generated according to $\theta_l \in [0, \pi)$ and $r_l \in [Z_1, 1.2Z_2]$ m. Each element in \mathbf{F} follows a complex Gaussian distribution $\mathcal{CN}(0, 1/N)$. Note that the sparsifying dictionary \mathbf{D}_{r_p} is dependent on r_p . Here we consider four different cases where r_p is set to $r_p = 20$ m, $r_p = 50$ m, $r_p = 80$ m, and r_p is randomly selected from the interval $[Z_1, Z_2]$ m, where $Z_1 = 2.16$ and $Z_2 = 97.54$. The normalized mean square error (NMSE) is used as a metric to evaluate the accuracy of the estimated channel vector, which is defined as

$$\text{NMSE} \triangleq \mathbb{E} \left(\frac{\|\mathbf{h} - \hat{\mathbf{h}}\|_2^2}{\|\mathbf{h}\|_2^2} \right) \quad (112)$$

with \mathbf{h} and $\hat{\mathbf{h}}$ being, respectively, the true channel and the estimated channel. The NMSE of the channel is obtained by averaging over 1000 Monte Carlo runs.

We first compare the mutual coherence of the sensing matrix constructed by our method and that constructed by the polar-domain method. The mutual coherence of a matrix is defined as the largest coherence of any two different columns of a matrix. Fig. 4 illustrates the mutual coherence of the sensing matrices used in the polar-domain based method and our proposed method. These results are based on 1000 independent realizations of \mathbf{F} . Clearly, the sensing matrix constructed by our proposed method is more likely to have a lower mutual coherence compared to the sensing matrix used by the polar-domain based method, indicating that our sensing matrix is more favorable for compressive sensing. This result

demonstrates the superiority of our sparse representation over the polar-domain representation.

Fig. 5a depicts the NMSEs as a function of the number of measurements T , where the SNR is set to 5dB. It can be observed that the proposed method can achieve a lower NMSE than the polar-domain on-grid and off-grid channel estimation methods. The performance gap is more pronounced when the number of measurements is small. Fig. 5b shows the NMSEs versus SNR, with T set to $T = 80$. From Fig. 5b, we see that our method provides a reliable channel estimate as long as the SNR is above 0dB, while the polar-domain method requires a higher SNR level to achieve a satisfactory performance. This result, again, demonstrates the superiority of this newly discovered sparse representation over the polar-domain representation. Also, our method exhibits a lower sensitivity to the choice of r_p , yielding similar NMSE results across different values of r_p .

VIII. CONCLUSIONS

We investigated the hybrid near/far-field channel estimation problem for mmWave/THz systems with an ELAA. We proposed a novel sparse representation for hybrid near/far-field channels by introducing a special distance-dependent dictionary matrix. Through theoretical analysis, we discovered that the hybrid near/far-field channel admits a block-sparse structure on the constructed dictionary matrix. By leveraging this block sparsity, the hybrid near/far-field channel estimation problem can be converted into a block-sparse signal recovery problem, efficiently solvable via existing block-sparse compressed sensing method. Simulation results were provided to corroborate our theoretical results and illustrate the channel estimation performance of the proposed method. These results demonstrated that our proposed method presents a clear performance advantage over state-of-the-art hybrid near/far channel estimation methods that are developed based on the polar domain representation.

APPENDIX A PROOF OF PROPOSITION 3

Based on the definition of $C(x)$, we have

$$\begin{aligned} & C(x + \Delta) - C(x) \\ &= \int_x^{x+\Delta} \cos(t^2) dt \\ &= \int_x^{x+\Delta} \frac{1}{2t} d(\sin(t^2)) \\ &\stackrel{(a)}{=} \frac{\sin(t^2)}{2t} \Big|_{t=x}^{t=x+\Delta} + \int_x^{x+\Delta} \frac{\sin(t^2)}{2t^2} dt \end{aligned} \quad (113)$$

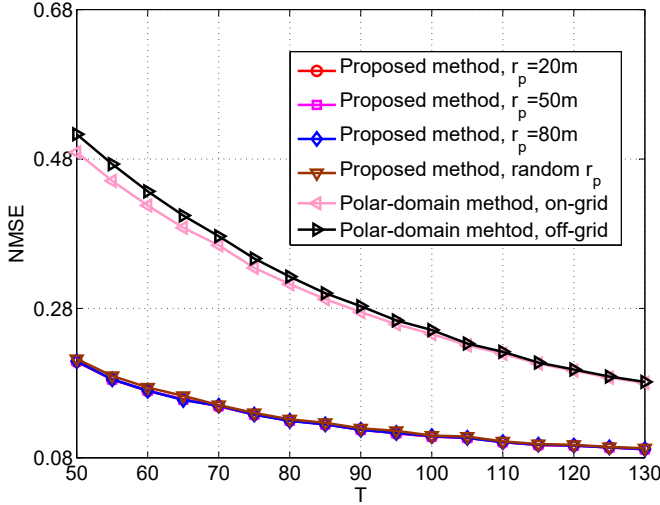
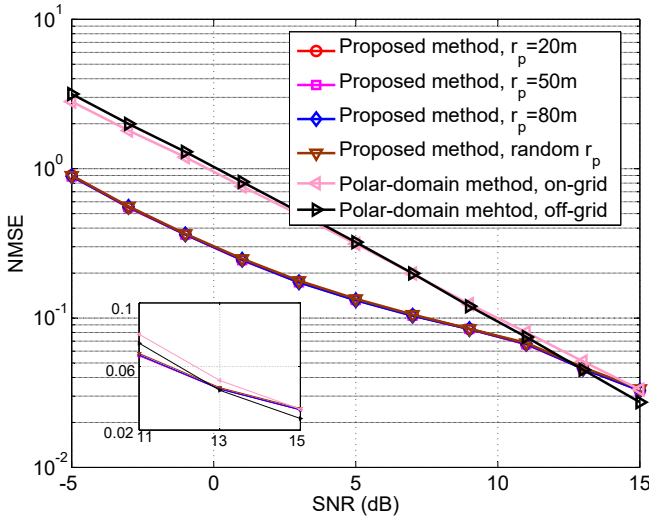
(a) NMSEs of respective methods versus T when SNR = 5dB(b) NMSEs of respective methods versus SNR when $T = 80$

Fig. 5: The NMSE of the estimated channel under different scenarios

where in (a) we utilize the integration by parts. Therefore, $|C(x + \Delta) - C(x)|$ can be expressed by

$$\begin{aligned}
 & |C(x + \Delta) - C(x)| \\
 & \leq \left| \frac{\sin((x + \Delta)^2)}{2(x + \Delta)} \right| + \left| \frac{\sin(x^2)}{2x} \right| + \int_x^{x+\Delta} \left| \frac{\sin(t^2)}{2t^2} \right| dt \\
 & \leq \frac{1}{2(x + \Delta)} + \frac{1}{2x} + \int_x^{x+\Delta} \frac{1}{2t^2} dt \\
 & = \frac{1}{x}
 \end{aligned} \tag{114}$$

The case for (55) can be similarly verified. This completes the proof.

APPENDIX B PROOF OF THEOREM 4

Before proving this theorem, we have the following propositions:

Proposition 5: Each element in $\Psi \in \mathbb{C}^{T \times N}$ follows $\mathcal{CN}(0, 1/N)$ with overwhelming probability. Also entries of Ψ are mutually independent.

Proof: See Appendix C. \blacksquare

Proposition 6 ([35], [37]): Consider a random Gaussian matrix \mathbf{D} of size $n \times N$ and block k -sparse signals over $\mathcal{I} = \{d_1 = d, \dots, d_M = d\}$, where $N = Md$ for some integer M . Let $t > 0$ and $0 < \xi < 1$ be constant numbers. If

$$n \geq \frac{36}{7\xi} \left(\ln(2L) + kd \ln \left(\frac{12}{\xi} \right) + t \right) \tag{115}$$

where $L = \binom{M}{k}$, then \mathbf{D} satisfies the block-RIP (108) with restricted isometry constant $\xi_{k, \mathcal{I}} = \xi$, with probability at least $1 - e^{-t}$.

It is known that α_{r_p} is block ϱ -sparse vector over \mathcal{I} defined in (109). Directly applying Proposition 5 and Proposition 6 will lead to the result that if the number of observations T satisfies

$$T \geq \frac{36}{7\xi} \left(\ln \left(\frac{\sqrt{N}}{\varrho} \right) + \varrho \sqrt{N} \ln \left(\frac{12}{\xi} \right) + \ln 2 + t \right) \tag{116}$$

then Ψ satisfies the block-RIP (108) with restricted isometry constant $\xi_{\varrho, \mathcal{I}} = \xi$, with probability at least $1 - e^{-t}$. In addition, based on the Stirling's formula, we have

$$\binom{\sqrt{N}}{\varrho} \leq \left(\frac{e\sqrt{N}}{\varrho} \right)^\varrho \tag{117}$$

Combining (116) and (117) together will complete our proof.

APPENDIX C PROOF OF PROPOSITION 5

The (i, j) th element of Ψ , denoted by ψ_{ij} is defined by

$$\begin{aligned}
 \psi_{ij} &= \mathbf{F}(i, :) \mathbf{D}_{r_p}(:, j) \\
 &= \sum_{n=1}^N \mathbf{F}(i, n) \mathbf{D}_{r_p}(n, j) \\
 &\triangleq \sum_{n=1}^N z_n
 \end{aligned} \tag{118}$$

where $z_n \triangleq \mathbf{F}(i, n) \mathbf{D}_{r_p}(n, j)$. Apparently, we have

$$\mathbb{E}(z_n) = 0 \tag{119}$$

$$\mathbb{V}(z_n) = \frac{|\mathbf{D}_{r_p}(n, j)|^2}{N} \tag{120}$$

In addition, due to the fact that $\mathbf{F}(i, n_1)$ and $\mathbf{F}(i, n_2)$ are independent, z_{n_1} and z_{n_2} are independent. Therefore, ψ_{ij} is a sum of i.i.d zero-mean random variables $\{z_n\}_{n=1}^N$. According to the central limit theorem (CLT), we have

$$\psi_{ij} \stackrel{(c)}{\sim} \mathcal{CN} \left(0, \frac{\sum_{n=1}^N |\mathbf{D}_{r_p}(n, j)|^2}{N} \right) \tag{121}$$

where $\overset{(c)}{\rightsquigarrow}$ means “converges to a distribution”.

Furthermore, consider two different elements in Ψ , i.e., $\psi_{i_1 j_1}$ and $\psi_{i_2 j_2}$ with $i_1 \neq i_2$ and meanwhile $j_1 \neq j_2$, which are expressed as

$$\psi_{i_1 j_1} = \mathbf{F}(i_1, :) \mathbf{D}_{r_p}(:, j_1) \quad (122)$$

$$\psi_{i_2 j_2} = \mathbf{F}(i_2, :) \mathbf{D}_{r_p}(:, j_2) \quad (123)$$

Due to the fact that $\mathbf{F}(i_1, :)$ and $\mathbf{F}(i_2, :)$ are independent and meanwhile $\mathbf{D}_{r_p}(:, j_1)$ and $\mathbf{D}_{r_p}(:, j_2)$ are mutual orthogonal, $\psi_{i_1 j_1}$ and $\psi_{i_2 j_2}$ are mutually independent. This can be further identified via checking the mutual information of $\psi_{i_1 j_1}$ and $\psi_{i_2 j_2}$. This ends our proof.

REFERENCES

- [1] Y. Yuan, Y. Zhao, B. Zong, and S. Parolari, “Potential key technologies for 6G mobile communications,” *Science China Information Sciences*, vol. 63, pp. 1–19, 2020.
- [2] B. Ji, Y. Han, S. Liu, F. Tao, G. Zhang, Z. Fu, and C. Li, “Several key technologies for 6G: Challenges and opportunities,” *IEEE Communications Standards Magazine*, vol. 5, no. 2, pp. 44–51, 2021.
- [3] C.-X. Wang, X. You, X. Gao, X. Zhu, Z. Li, C. Zhang, H. Wang, Y. Huang, Y. Chen, H. Haas *et al.*, “On the road to 6G: Visions, requirements, key technologies and testbeds,” *IEEE Communications Surveys & Tutorials*, 2023.
- [4] M.-X. Chang, “A new derivation of least-squares-fitting principle for OFDM channel estimation,” *IEEE Transactions on Wireless Communications*, vol. 5, no. 4, pp. 726–731, 2006.
- [5] E. Karimi, “Tracking performance of least squares MIMO channel estimation algorithm,” *IEEE Transactions on Communications*, vol. 55, no. 11, pp. 2201–2209, 2007.
- [6] J.-C. Lin, “Least-squares channel estimation for mobile OFDM communication on time-varying frequency-selective fading channels,” *IEEE Transactions on Vehicular Technology*, vol. 57, no. 6, pp. 3538–3550, 2008.
- [7] J. Lee, G.-T. Gil, and Y. H. Lee, “Channel estimation via orthogonal matching pursuit for hybrid MIMO systems in millimeter wave communications,” *IEEE Transactions on Communications*, vol. 64, no. 6, pp. 2370–2386, 2016.
- [8] A. C. Gurbuz, Y. Yapici, and I. Guvenc, “Sparse channel estimation in millimeter-wave communications via parameter perturbed omp,” in *2018 IEEE International Conference on Communications Workshops (ICC Workshops)*. IEEE, 2018, pp. 1–6.
- [9] H. Kim, G.-T. Gil, and Y. H. Lee, “Two-step approach to time-domain channel estimation for wideband millimeter wave systems with hybrid architecture,” *IEEE Transactions on Communications*, vol. 67, no. 7, pp. 5139–5152, 2019.
- [10] S. Srivastava, A. Mishra, A. Rajorija, A. K. Jagannatham, and G. Ascheid, “Quasi-static and time-selective channel estimation for block-sparse millimeter wave hybrid mimo systems: Sparse bayesian learning (sbl) based approaches,” *IEEE Transactions on Signal Processing*, vol. 67, no. 5, pp. 1251–1266, 2018.
- [11] X. Wu, S. Ma, X. Yang, and G. Yang, “Clustered sparse bayesian learning based channel estimation for millimeter-wave massive mimo systems,” *IEEE Transactions on Vehicular Technology*, vol. 71, no. 12, pp. 12 749–12 764, 2022.
- [12] C. Huang, L. Liu, C. Yuen, and S. Sun, “Iterative channel estimation using lse and sparse message passing for mmwave mimo systems,” *IEEE Transactions on Signal Processing*, vol. 67, no. 1, pp. 245–259, 2018.
- [13] F. Bellili, F. Sahrabi, and W. Yu, “Generalized approximate message passing for massive MIMO mmwave channel estimation with laplacian prior,” *IEEE Transactions on Communications*, vol. 67, no. 5, pp. 3205–3219, 2019.
- [14] N. J. Myers and R. W. Heath, “Message passing-based joint CFO and channel estimation in mmWave systems with one-bit adcs,” *IEEE Transactions on Wireless Communications*, vol. 18, no. 6, pp. 3064–3077, 2019.
- [15] Y. Tsai, L. Zheng, and X. Wang, “Millimeter-wave beamformed full-dimensional mimo channel estimation based on atomic norm minimization,” *IEEE Transactions on Communications*, vol. 66, no. 12, pp. 6150–6163, 2018.
- [16] C. Hu, L. Dai, T. Mir, Z. Gao, and J. Fang, “Super-resolution channel estimation for mmwave massive MIMO with hybrid precoding,” *IEEE Transactions on Vehicular Technology*, vol. 67, no. 9, pp. 8954–8958, 2018.
- [17] Z. Zhou, J. Fang, L. Yang, H. Li, Z. Chen, and R. S. Blum, “Low-rank tensor decomposition-aided channel estimation for millimeter wave mimo-ofdm systems,” *IEEE Journal on Selected Areas in Communications*, vol. 35, no. 7, pp. 1524–1538, 2017.
- [18] X. Li, J. Fang, H. Li, and P. Wang, “Millimeter wave channel estimation via exploiting joint sparse and low-rank structures,” *IEEE Transactions on Wireless Communications*, vol. 17, no. 2, pp. 1123–1133, 2017.
- [19] M. Cui and L. Dai, “Channel estimation for extremely large-scale MIMO: Far-field or near-field?” *IEEE Transactions on Communications*, vol. 70, no. 4, pp. 2663–2677, 2022.
- [20] X. Wei and L. Dai, “Channel estimation for extremely large-scale massive MIMO: Far-field, near-field, or hybrid-field?” *IEEE Communications Letters*, vol. 26, no. 1, pp. 177–181, 2021.
- [21] A. Lee, H. Ju, S. Kim, and B. Shim, “Intelligent near-field channel estimation for terahertz ultra-massive mimo systems,” in *GLOBECOM 2022-2022 IEEE Global Communications Conference*. Rio de Janeiro, Brazil, 2022, pp. 5390–5395.
- [22] X. Zhang, Z. Wang, H. Zhang, and L. Yang, “Near-field channel estimation for extremely large-scale array communications: A model-based deep learning approach,” *IEEE Communications Letters*, 2023.
- [23] H. Lei, J. Zhang, H. Xiao, X. Zhang, B. Ai, and D. W. K. Ng, “Channel estimation for xl-mimo systems with polar-domain multi-scale residual dense network,” *IEEE Transactions on Vehicular Technology*, 2023.
- [24] Y. Chen, L. Yan, and C. Han, “Hybrid spherical-and planar-wave modeling and DCNN-powered estimation of terahertz ultra-massive mimo channels,” *IEEE Transactions on Communications*, vol. 69, no. 10, pp. 7063–7076, 2021.
- [25] S. Yang, X. Chen, Y. Xiu, W. Lyu, Z. Zhang, and C. Yuen, “Performance bounds for near-field localization with widely-spaced multi-subarray mmWave/THz MIMO,” *arXiv preprint arXiv:2309.05944*, 2023.
- [26] S. Tarboush, A. Ali, and T. Y. Al-Naffouri, “Cross-field channel estimation for ultra massive-MIMO THz systems,” *IEEE Transactions on Wireless Communications*, 2024.
- [27] H. Wang, J. Fang, and J. Wang, “Compressive near/far-field channel estimation for mmwave/thz systems with extremely large antenna arrays,” in *GLOBECOM 2023 - 2023 IEEE Global Communications Conference*, 2023, pp. 2354–2359.
- [28] R. W. Heath, N. Gonzalez-Prelcic, S. Rangan, W. Roh, and A. M. Sayeed, “An overview of signal processing techniques for millimeter wave MIMO systems,” *IEEE Journal of Selected Topics in Signal Processing*, vol. 10, no. 3, pp. 436–453, 2016.
- [29] B. C. Berndt, R. J. Evans, and K. S. Williams, *Gauss and Jacobi sums*. Wiley, 1998.
- [30] R. Paris, “An asymptotic expansion for the generalised quadratic gauss sum,” *Applied Mathematical Sciences*, vol. 2, pp. 577–592, 2008.
- [31] M. R. Zaghoul and L. Alrawas, “Calculation of fresnel integrals of real and complex arguments up to 28 significant digits,” *Numerical Algorithms*, pp. 1–19, 2023.
- [32] R. G. Baraniuk, V. Cevher, M. F. Duarte, and C. Hegde, “Model-based compressive sensing,” *IEEE Transactions on Information Theory*, vol. 56, no. 4, pp. 1982–2001, 2010.
- [33] Y. C. Eldar, P. Kuppinger, and H. Bolekski, “Block-sparse signals: Uncertainty relations and efficient recovery,” *IEEE Transactions on Signal Processing*, vol. 58, no. 6, pp. 3042–3054, 2010.
- [34] J. Fang, Y. Shen, H. Li, and P. Wang, “Pattern-coupled sparse Bayesian learning for recovery of block-sparse signals,” *IEEE Transactions on Signal Processing*, vol. 63, no. 2, pp. 360–372, 2014.
- [35] Y. C. Eldar and M. Mishali, “Robust recovery of signals from a structured union of subspaces,” *IEEE Transactions on Information Theory*, vol. 55, no. 11, pp. 5302–5316, 2009.
- [36] M. R. Akdeniz, Y. Liu, M. K. Samimi, S. Sun, S. Rangan, T. S. Rappaport, and E. Erkip, “Millimeter wave channel modeling and cellular capacity evaluation,” *IEEE Journal on Selected Areas in Communications*, vol. 32, no. 6, pp. 1164–1179, 2014.
- [37] T. Blumensath and M. E. Davies, “Sampling theorems for signals from the union of finite-dimensional linear subspaces,” *IEEE Transactions on Information Theory*, vol. 55, no. 4, pp. 1872–1882, 2009.